Photocatalytic Reduction of CO$_2$ from Simulated Flue Gas with Colored Anatase

Yebin Guan [1,2], Ming Xia [1], Alessandro Marchetti [1] (iD), Xiaohong Wang [2], Weicheng Cao [1], Hanxi Guan [1] and Xueqian Kong [1,*]

[1] Center for Chemistry of Novel & High-Performance Materials, and Department of Chemistry, Zhejiang University, Hangzhou 310027, China; guanyb@aqnu.edu.cn (Y.G.); xiaming301@126.com (M.X.); alexmar983@yahoo.it (A.M.); caowc@zju.edu.cn (W.C.); guanhx0123@zju.edu.cn (H.G.)

[2] Anhui Key Laboratory of Functional Coordination Compounds, School of Chemistry and Chemical Engineering, Anqing Normal University, Anqing 246011, China; wangxiaohong@aqnu.edu.cn

[*] Correspondence: kxq@zju.edu.cn; Tel.: +86-571-8795-3189

Abstract: Photocatalytic reduction with sunlight is an economical and promising advanced approach for reducing the excessive emissions of CO$_2$ from the combustion of fossil fuels. Aimed at practical applications, a type of inexpensive colored anatase material was used to evaluate CO$_2$ photoreduction performance on a platform with a continuous flow of gas mixtures (10 vol % CO$_2$, 90% N$_2$), which resembles realistic flue gas conditions. The results showed an enhanced photocatalytic activity compared with standard P25 and significant improvement over pristine anatase. Based on a series of characterization techniques, we propose that the oxygen vacancies and surface hydroxyl groups on colored anatase can reduce the bandgap and assist the binding of CO$_2$ molecules. Our results showed that photoreduction of CO$_2$ is feasible under practical conditions, and the efficiency could be improved through modification of catalysts.

Keywords: photocatalytic reduction; TiO$_2$; anatase; CO$_2$; flue gas

1. Introduction

The excessive emissions of CO$_2$ generated by the combustion of fossil fuels have a prolonged consequence on the global climate [1]. For instance, as one of the major contributors to CO$_2$ emissions, thermal power stations emit 10–20 volume percent of CO$_2$ in their flue gas. Although major research efforts have been aimed at CO$_2$ capture and sequestration, direct conversion of CO$_2$ into useable chemicals is a desired, yet more challenging approach. Various chemical or electrochemical processes have been developed to reduce CO$_2$ to CO or hydrocarbon compounds [2–4]; however, due to the chemical inertness of CO$_2$, most strategies for CO$_2$ reduction can only be achieved at an unaffordable cost of energy or reagents. Alternatively, photocatalytic reduction of CO$_2$ with sunlight would be much more economical, and it is being actively researched [5]. However, current photocatalytic processes either use strong ultraviolet light, or additional sacrificial agents, or conditions far from the industrial processes, while the development of solar-active photocatalysts is still at its early stage.

Till now, a great quantity of works has been endeavored to explore photocatalysts for selective CO$_2$ transformations [6–9]. For instance, a novel molecular Ru(II)−Re(I) dinuclear complex photocatalytic system with high reduction ability of CO$_2$ and capture ability of CO$_2$ has been developed [6]. Rosenthal et al. developed an inexpensive bismuth-carbon monoxide evolving catalyst (Bi-CMEC), which can selectively catalyze the conversion of CO$_2$ to CO without the need for a costly supporting electrolyte [7]. BiFeO$_3$ and BiFeO$_3$/single-walled carbon nanotubes (SWCNTs) were prepared by the sol-gel method, and the modification of the catalysts by single-walled carbon nanotubes not only greatly improved the response to visible light, but also doubled the catalytic reduction yield of

CO_2 [8]. Among these, TiO_2-based photocatalysts have been most widely studied as photocatalyst with different crystalline forms or modifications [10–13], and they show considerable prospect for the selective transformation of CO_2 to CO, HCOOH, CH_3OH and CH_4 [14]. The P25 TiO_2 nanoparticles branded by Degussa, which have mixed phases of rutile and anatase, are the benchmark material with high photocatalytic performance. However, P25 is relatively expensive, which precludes its use on the scale required for fuel production. Alternatively, loading noble metals such as Pt, Au and Ag can enhance its activities of CO_2 photoreduction for commercial anatase or rutile materials, but the cost is also high. Therefore, the development of inexpensive photocatalysts that can promote the reduction of CO_2 to CO with high selectivity and efficiency is an important step for commercialization.

In this report, we evaluated the CO_2 photoreduction performance on a platform with a continuous flow of gas mixtures (10 vol % CO_2, 90% N_2 at 80 °C) that resembles realistic flue gas conditions. In such conditions, energy-intensive CO_2 separation processes [15] may be avoided. The conversion of CO_2 to CO can be achieved on titanium oxide catalysts with additional water under xenon light in the UV-visible or visible-only range. Carbon monoxide is a key chemical feedstock and a component of syngas, which can be further converted to liquid hydrocarbon fuels. In order to reduce the cost for large-scale application, a colored anatase (g-anatase) material has been prepared, which showed a comparable photocatalytic activity with standard P25 and significant improvement over pristine anatase. Based on characterizations by X-ray diffraction (XRD), transmission electron microscopy (TEM), X-ray photoelectron spectroscopy (XPS), electron paramagnetic resonance (EPR), Fourier transforming infrared spectroscopy (FT-IR) and solid-state nuclear magnetic resonance (SSNMR), we propose that oxygen vacancies and surface hydroxyl groups on colored anatase can reduce the bandgap and assist the binding of CO_2 molecules. Our results showed that photo-reduction of CO_2 is feasible under flue gas conditions, and the efficiency could be improved through modification of catalysts.

2. Results and Discussion

2.1. CO₂ Photoreduction Performance

A number of photocatalysts has been reported for the conversion of CO_2 into CO under continuous flow conditions (Table 1) [11–13,16,17]. However, for flue gas, CO_2 concentration is around 10% in volume. If we used pure CO_2 for reduction, this would demand either intensive energy or special adsorbents for CO_2 separation [18]. For practical and economic considerations, we performed photocatalysis using low concentration CO_2 just like flue gas (i.e., 90% N_2 and 10% CO_2). Other features of flue gas such as temperature and humidity have also been simulated [19]. The temperature of the reaction chamber was maintained at 80 °C, which also approximates the temperature of flue gas. A certain degree of humidity was maintained with added water, and the gas in the reaction chamber was internally cycled with a pump to assist the flow of flue gas. We used xenon light with either the UV or UV-visible range to excite anatase and colored-anatase samples. Under our experimental conditions, CO is the primary product that we detected through an on-line gas chromatography.

Table 1. A list of defective TiO_2 catalytic performance for CO_2 photoreduction.

Catalysts	Light Source	CO_2 Concentration	CO Production (μmol/h)	Reference
TiO_{2-x}/exposed {001}/{101} facets (through $NaBH_4$ reduction)	UV: 100-W mercury vapor lamp; visible: 450-W Xe lamp (λ > 400 nm)	4 mL/min CO_2 + H_2O continuous flow	UV:CO = 0.44, Vis:CO = 0.208	[13]
Brookite TiO_{2-x} (thermal treatment in He)	150-W solar simulator	2 mL/min, CO_2 + H_2O continuous flow	CO + CH_4 = 0.315	[11]
2.5 at% Co-TiO_2 (sol-gel method)	Visible light of 300-W Xe arc lamp with an L-42 glass filter	3 mL DI H_2O and 80 kPa CO_2 gas	CO = 0.194, CH_4 = 0.009	[16]
4% Cu@TiO_2 (annealing at 450 °C for 2 h in high vacuum)	Visible light of 500-W Xe lamp (λ > 400 nm)	CO_2 generated from $NaHCO_3$/H_2SO_4 reaction	CO = 0.162, CH_4 = 0.027	[12]
10% I-TiO_2 hydrolysis of titanium isopropoxide (TTIP) in iodic acid solution followed by hydrothermal treatment	Visible light of 150-W solar simulator	CO_2 + H_2O mix gas	CO = 0.48	[17]

The production of CO (μmol/g) during a 6-h photo-illumination period was calculated, as shown in Figure 1. It can be seen that the CO production on colored-anatase greatly increased; the maximum CO production rate was up to 4.99 μmol g^{-1} (i.e., a rate of 0.83 μmol g^{-1} h^{-1}) under UV-visible light irradiation (the UV-vis column in Figure 1), which is circa 10.7-times that of anatase and higher than P25 [20]. If the UV light (wavelength smaller than 400 nm) was cut off, the overall production of CO decreased (the UV cut400 column in Figure 1), and this suggests that UV-light plays an important role in the catalyzing process. However, even with visible light, the colored anatase can still produce about 1.2 μmol g^{-1} CO (i.e., a rate of 0.2 μmol g^{-1} h^{-1}), which is ~20% higher than P25. Although such a conversion rate of CO_2 into CO does not seem so impressive compared to the literature, it should be pointed out that our experiments were performed with more stringent conditions at a much lower CO_2 concentration. As a proof of concept experiment, our results have confirmed the feasibility of direct photocatalytic conversion of CO_2 with flue gas for the first time. Our work also suggests that improvement of the existing catalysts can greatly benefit the conversion efficiency. Therefore, in the following section, we carried out further study on the colored anatase, which is also introduced in this work.
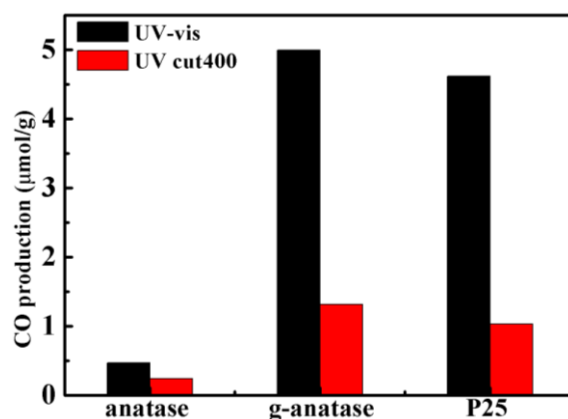

Figure 1. The histogram of CO maximum output with 6 h using anatase, colored anatase and P25 as the catalysts. g-anatase, gray anatase.

2.2. Characterization of Colored Anatase

It has been demonstrated that a higher density of oxygen vacancies in colored TiO_2 could contribute to enhanced photocatalytic activity [21–23]. For example, black TiO_2 nanoparticles with a defective core/disordered shell structure exhibited a bandgap of only 1.85 eV, and the bandgap narrowing is dictated by the synergistic presence of oxygen vacancies and surface disorder [22]. Figure 2a shows the commercial anatase (white color) and the treated anatase powder (gray color, named g-anatase). This distinct change of color indicates that the band structure of anatase nanocrystals has been modified by the $NaBH_4$ reduction treatment. The XRD patterns in Figure 2b showed that the gray TiO2 kept the anatase phase, suggesting this reduction treatment did not alter the crystalline core. The diffuse reflectance UV-Vis spectrum of colored anatase (Figure 2c) clearly shows a broad absorption from 400 nm to the near-infrared region. The relationship between absorbance (Ahv)$^{1/2}$ and photo energy (hv) is shown in Figure 2d, and the bandgap of g-anatase is calculated to be 2.04 eV (compared to 2.97 eV for pristine anatase), which allows the adsorption of a large part of visible light.
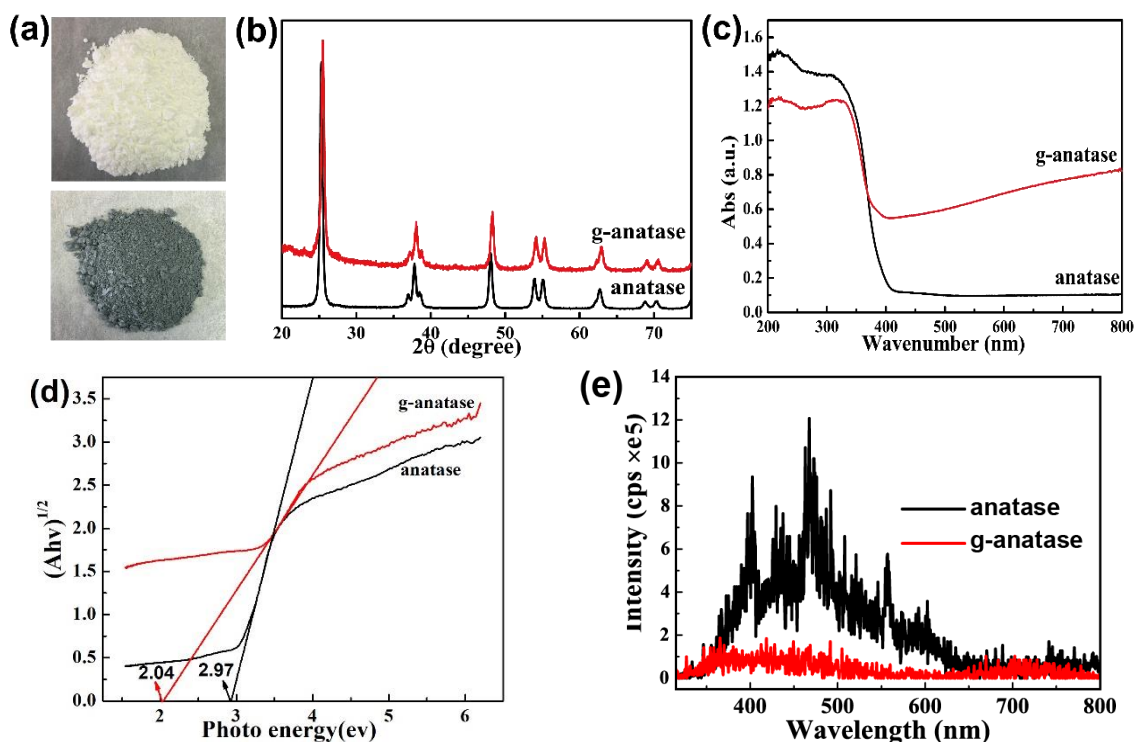
Figure 2. (**a**) Images of anatase (top) and colored anatase (bottom), (**b**) XRD patterns, (**c**) diffuse reflectance UV-Vis spectra, (**d**) relationship between (Ahν) $^{1/2}$ and hν and (**e**) photoluminescence (PL) spectra of anatase and colored anatase.

A photoluminescence (PL) experiment was used to track the recombination of charged carriers freed by photo excitation (325 nm) [24,25]. The PL intensity of colored anatase is much weaker compared to anatase, which indicates that the recombination rate of photo-generated electrons and holes had been reduced considerably (Figure 2e) [26]. Together, the UV-Vis and PL experiments explain the photoactivity of colored anatase in the visible and UV-visible range. In order to fully address the mechanism of its enhanced CO_2 reduction performance, we conducted further structural characterizations by TEM, EDX, XPS, IR, SSNMR, TG and CO_2 adsorption and desorption experiments.

TEM revealed that the average diameter of colored anatase nanocrystals is about 25 nm (Figure 3c), similar to pristine anatase (Figure 3a). Before the reduction treatment, TiO_2 nanocrystals exhibit a highly crystalline nature and well resolved lattice features throughout the whole particles (Figure 3b). However, after the reduction treatment, the anatase nanocrystals show a crystallized core with a disordered outer layer, which forms a shell of about 1.5 nm in thickness, as shown by the black arrows in Figure 3d, and this confirms that the obtained sample has a $TiO_2@TiO_{2-x}$ core/shell structure feature [27]. The corresponding EDX spectrum (Figure 4) showed that there are only Ti and O elements existing in the g-anatase (C and Cu are from the supporting super-thin carbon-coated copper grid). In addition, the atomic ratio of Ti to O is below the stoichiometric ratio of two, which further proved the formation of the amorphous shell.

The high-resolution spectra of Ti2p XPS of commercial anatase and colored anatase are shown in Figure 5a. The Ti2p 3/2 and Ti2p 1/2 peaks centered at the binding energies of 460.5 and 466.2 eV are typical characteristics of the Ti^{4+}–O bonds in anatase. Such peaks shift nevertheless to lower binding energies of 460.0 and 465.9 eV in the colored anatase, which indicates that Ti^{3+} species may have appeared in the colored anatase sample, as previously reported [28,29].
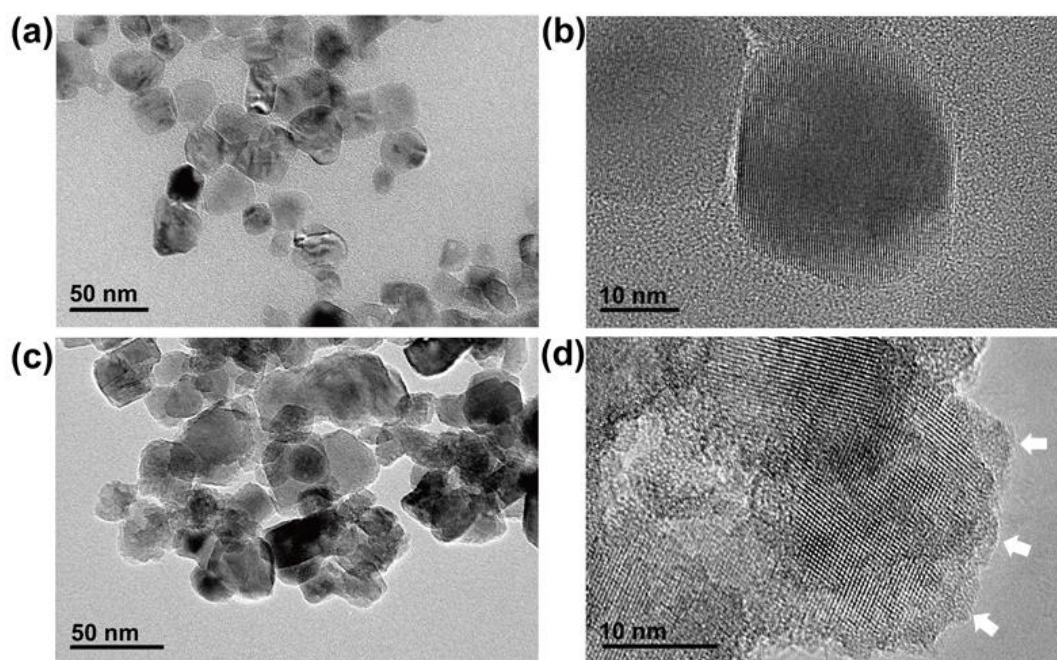
Figure 3. (**a**,**c**) TEM and (**b**,**d**) HRTEM images of anatase and colored anatase nanocrystals.

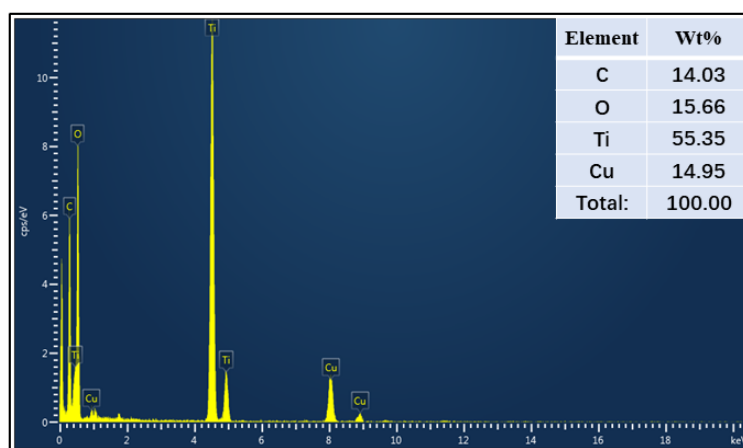| Element	Wt%
C	14.03
O	15.66
Ti	55.35
Cu	14.95
Total:	100.00

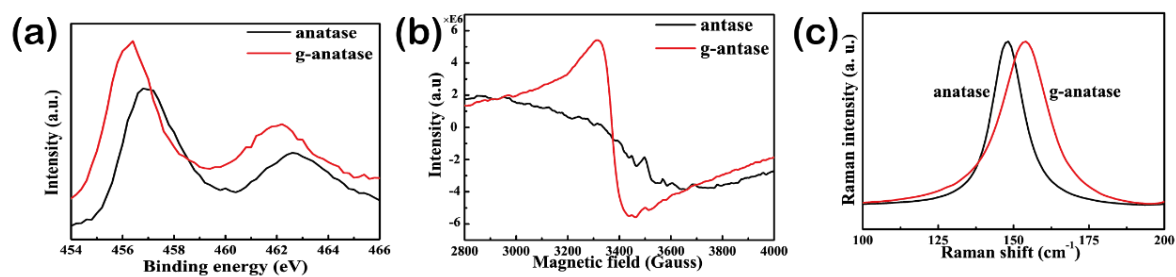**Figure 4.** EDX of colored anatase nanocrystals.

Figure 5. (**a**) High-resolution XPS spectra of Ti 2p, (**b**) electron paramagnetic resonance (EPR) and (**c**) Raman spectra of anatase and colored anatase.

The EPR technique was further employed to analyze the Ti^{3+}-related vacancy defects. From Figure 5b, there is an obvious signal at g = 2.058 for the g-anatase sample, which can be attributed to oxygen vacancy [30]; therefore, the defects probed from slow negative annihilation

spectroscopy may be considered to be oxygen-related vacancy, which is consistent with the XPS results. Oxygen-related vacancy defects mainly exist in the bulk (or surface) lattice of the TiO_2 samples after reduction treatment. Raman spectroscopy (Figure 5c) reveals that the strongest vibration mode area (Eg) at 144 cm^{-1} had a significant peak broadening and blue shifting after reduction treatment, compared with commercial anatase. The peak broadening effect and shift have been observed in several recent studies on hydrogenated TiO_2 [22,30–32], which are attributed to the presence of lattice disorder resulting from phonon confinement or nonstoichiometry as the result of oxygen vacancy (VO) doping.

FT-IR spectra (Figure 6a,b) of both white and colored anatase were recorded to investigate light absorption in the mid-infrared light region, from 400 cm^{-1}–4000 cm^{-1}. This allowed gaining further insight into the molecular-level alterations induced by the hydrogenation process. Similar absorption features can be detected in the two samples, namely the OH of H_2O bands near 1635 cm^{-1} and 3400 cm^{-1} and the characteristic wide band in the region 510~650 cm^{-1}, which is due to the symmetric stretching vibrations of the Ti–O bonds of the TiO_4 tetrahedra. The differences between spectra (Figure 6b) reveal that hydrogenation leads to additional absorption peaks at 3648, 3672, and 3691 cm^{-1}, which can be associated with tetrahedral coordinated vacancies and designated as $Ti^{4+}-OH$ [33]. Moreover, hydrogenation leads to another new absorbance at 3710 cm^{-1}, corresponding to terminal OH groups [34], which could be attributed to the hydrogen atoms embedded in the TiO_2 network.
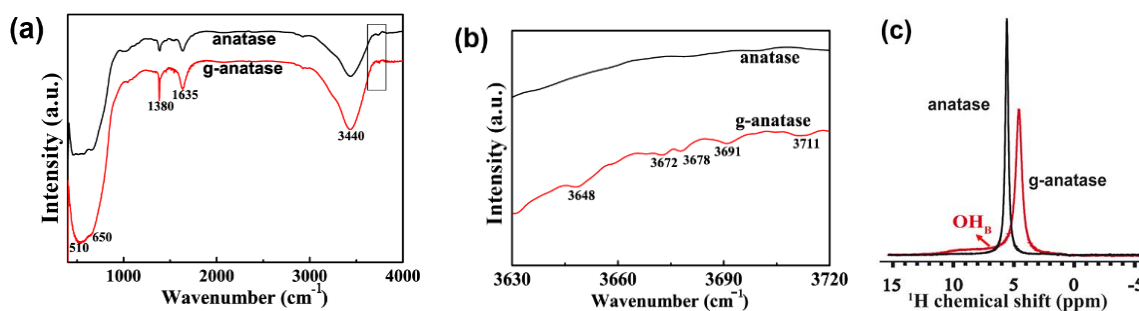

Figure 6. (**a**,**b**) FT-IR spectra and (**c**) ^{1}H solid-state NMR spectra of anatase and colored anatase.

Ultra-fast magic-angle spinning (MAS) solid-state NMR spectroscopy is a crucial tool for the effective characterization of the hydrogen species present on nanocrystals. We performed ^{1}H NMR measurements of anatase and colored anatase at an MAS rate of 60 kHz, as shown in Figure 6c. The dominant peaks at 5.5 and 4.8 ppm in anatase and colored anatase, respectively, can be assigned to the isolated water molecules trapped in anatase crystal defects. Such sharp ^{1}H peaks, which were also observed at the lower spinning speed of 12 kHz, are features of weak $^1H-^1H$ dipolar coupling. It is unlikely to be mobile water, however, as the sample has been treated in vacuum at elevated temperatures. Different from anatase, the colored anatase showed also a relatively broad signal at 6.7 ppm corresponding to bridging (i.e., non-terminal) surface hydroxyl groups (marked in Figure 6c as OH_B), which is consistent with the 3648 cm^{-1} FT-IR signal [35].

CO_2 adsorption and desorption curves of anatase and colored anatase are shown in Figure 7a. One can find that both CO_2 adsorbed and desorbed capacities detected at the low pressure range ($P/P_0 < 0.2$) on g-anatase nanocrystals are higher than those on anatase nanocrystals; this feature is probably closely related to the more exposed alkaline sites, namely Ti^{3+} vacancies on g-anatase nanocrystals, which can absorb more CO_2 molecules [36]. The TGA curve reported in Figure 7b shows that the continuous weight losses of the anatase and g-anatase samples are 2.36 and 3.65% before 350 °C, which can be ascribed to the adsorbed water evaporation. Obviously, the greater weight loss of g-anatase indicates that more water molecules are adsorbed on the surface of the crystals, which is probably closely associated with the amorphous shell of colored anatase [37].
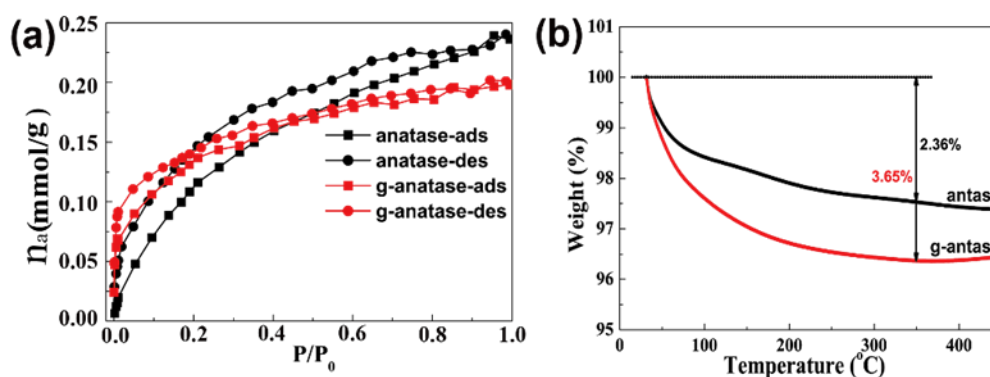
Figure 7. (**a**) CO_2 adsorption and desorption curves and (**b**) TGA curves of anatase and colored anatase samples.

3. Experimental Section

3.1. Surface Defective Anatase Preparation

Anatase (99.8%, 25 nm), $NaBH_4$ (98%) and ethanol (AR) were purchased from Aladdin Reagent Comp. (Shanghai, China) and used without purification. The surface defective anatase preparation process is reported elsewhere [20]. Typically, 2.40 g of anatase powder and 0.90 g of $NaBH_4$ were mixed thoroughly with 20 min if grinding. The mixture was then placed into a porcelain capsule inside a tubular furnace in Ar atmosphere and heated from ambient temperature with a rate of 10 °C/min until it reached 400 °C, then maintained at this level for 120 min. After self-cooling to ambient temperature, the obtained gray powder was washed seven times alternately with deionized water and ethanol to remove unreacted $NaBH_4$, then dried at 60 °C in air.
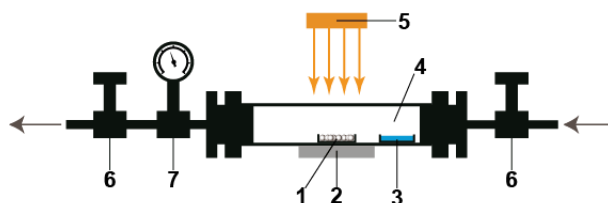
3.2. Sample Characterization

Diffraction patterns were collected using an X-ray diffractometer (XRD) (Bruker AXS D8 Focus, Karlsruhe, Germany) with Cu Ka radiation (λ = 1.54056 A). The UV-Vis absorption spectra were recorded on a Shimadzu UV 2600 UV/Vis spectrophotometer (SHIMADZU Corporation, Kyoto, Japan). Transmission electron microscope (TEM) images were taken using a JEOL 2100 operating at 200 kV (Japan Electron Optics Laboratory Co., Ltd., Kyoto, Japan). X-ray photoelectron spectra (XPS) analyses were recorded using an ESCALABMKII spectrometer with an AlKa (1486.6 eV) achromatic X-ray source (VG Scienta, East Sussex, UK). The EPR spectra were acquired using a Bruker EMX-8 spectrometer at 9.36 GHz at 298.5 K (Karlsruhe, Germany). Raman spectra were collected on a thermal dispersive spectrometer using laser light with an excitation wavelength of 532 nm at a laser power of 10 mW. ^1H SSNMR experiments were conducted at a probe temperature of 302 ± 1 K on an AVANCE 600-MHz wide bore spectrometer (Bruker, Karlsruhe, Germany) operating at 14.1 T (the Larmor frequency was 599.80 MHz for the proton) and equipped with a 1.3-mm triple-resonance magic angle spinning (MAS) probe. Free induction decays (FIDs) were not multiplied by an exponential anodization function before Fourier transformation. The spectrum of an empty NMR rotor was collected under the same conditions and subtracted to eliminate the contribution from background signals [35,38,39]. Chemical shifts were measured relative to secondary standard adamantane as an external reference [40,41].

3.3. The Gas-Solid Reaction System

The gas-solid reaction measurement is designed as shown in Scheme 1. A 300-W Xe lamp was used as the light source and eventually filtered to remove its UV part. As a preliminary step, we tested with GC/TCD-FID the eventual background level of carbon-containing products of a mixture of H_2O and He passing through the catalyst with the lamp on. This confirmed that CO_2 was indeed

the only carbon source. The production of CO during a given period was calculated by measuring its concentrations at the reactor outlet.

Scheme 1. Diagram of the photocatalytic equipment. (1) Quartz boat for the loading of the TiO_2 catalyst, (2) external heating sleeve, (3) Petri dish containing deionized water, (4) main device constituted by a high-permeability quartz tube and stainless seal flanges, (5) xenon light source, (6) needle valve for the control of the gas flow rate, (7) air gauge displaying the pressure variation in the reaction device. The arrows indicate the flow direction.

4. Conclusions

In summary, we firstly prepared the core/shell structure of the $TiO_2@TiO_{2-x}$ sample by mildly reducing commercial anatase. Such a colored anatase showed comparable photocatalytic activity towards CO_2 reduction under a simulated flue gas system. The enhanced activity is attributed to the formation of oxygen vacancies and Ti^{3+} on the amorphous surface shell, which promotes CO_2 activation under photo-illumination. Our work represents a further step to utilize post-combustion CO_2 in a sustainable manner, i.e., using sunlight and without further processing. Further refinement of reaction conditions and catalytic supports is still possible in order to improve the overall efficiency of photocatalysis

Author Contributions: X.K., Y.G. and M.X. conceived and designed the experiments; Y.G., M.X. and W.C. performed the experiments; M.X. and A.M. analyzed the data; H.G. and X.M. contributed reagents/materials/ analysis tools; Y.G. and X.K. wrote the paper.

Conflicts of Interest: The authors declare no conflict of interest.

References

1. Yu, J.G.; Low, J.X.; Xiao, W.; Zhou, P.; Jaroniec, M. Enhanced photocatalytic CO_2-reduction activity of anatase TiO_2 by coexposed {001} and {101} facets. *J. Am. Chem. Soc.* **2014**, *136*, 8839–8842. [CrossRef] [PubMed]
2. Zhu, Z.; Qin, J.; Jiang, M.; Ding, Z.; Hou, Y. Enhanced selective photocatalytic CO_2 reduction into CO over Ag/CdS nanocomposites under visible light. *Appl. Surf. Sci.* **2017**, *391*, 572–579. [CrossRef]
3. Tahir, M.; Tahir, B.; Amin, N.A.S.; Zakaria, Z.Y. Photo-induced reduction of CO_2 to CO with hydrogen over plasmonic Ag-NPs/TiO_2 NWs core/shell hetero-junction under UV and visible light. *J. CO2 Util.* **2017**, *18*, 250–260. [CrossRef]
4. Tahir, M.; Tahir, B.; Amin, N.A.S. Synergistic effect in plasmonic Au/Ag alloy NPs co-coated TiO_2 NWs toward visible-light enhanced CO_2 photoreduction to fuels. *Appl. Catal. B Environ.* **2017**, *204*, 548–560. [CrossRef]
5. House, R.L.; Iha, N.Y.M.; Coppo, R.L.; Alibabaei, L.; Sherman, B.D.; Kang, P.; Brennaman, M.K.; Hoertz, P.G.; Meyer, T.J. Artificial photosynthesis: Where are we now? Where can we go? *J. Photochem. Photobiol. C Photochem. Rev.* **2015**, *25*, 32–45. [CrossRef]
6. Nakajima, T.; Tamaki, Y.; Ueno, K.; Kato, E.; Nishikawa, T.; Ohkubo, K.; Yamazaki, Y.; Morimoto, T.; Ishitani, O. Photocatalytic reduction of low concentration of CO_2. *J. Am. Chem. Soc.* **2016**, *138*, 13818–13821. [CrossRef] [PubMed]

7. Medina-Ramos, J.; DiMeglio, J.L.; Rosenthal, J. Efficient reduction of CO_2 to CO with high current density using in situ or ex situ prepared Bi-Based materials. *J. Am. Chem. Soc.* **2014**, *136*, 8361–8367. [CrossRef] [PubMed]

8. Li, X.; He, S.Y.; Li, Z. Methanol synthesis in the catalytic reduction of CO_2 under the visible light by $BiFeO_3$ modified with carbon nanotubes. *J. Chin. Ceram. Soc.* **2009**, *37*, 1869–1872.

9. Ponzoni, C.; Rosa, R.; Cannio, M.; Buscaglia, V.; Finocchio, E.; Nanni, P.; Leonelli, C. Electrophoretic deposition of multiferroic $BiFeO_3$ submicrometric particles from stabilized suspensions. *J. Eur. Ceram. Soc.* **2012**, *33*, 1325–1333. [CrossRef]

10. Liu, G.D.; Xie, S.J.; Zhang, Q.H.; Tian, Z.F.; Wang, Y. Carbon dioxide-enhanced photosynthesis of methane and hydrogen from carbon dioxide and water over Pt-promoted polyaniline–TiO_2 nanocomposites. *Chem. Commun.* **2015**, *51*, 13654–13657. [CrossRef] [PubMed]

11. Liu, L.J.; Zhao, H.L.; Andino, J.M.; Li, Y. Photocatalytic CO_2 Reduction with H_2O on TiO_2 Nanocrystals: Comparison of Anatase, Rutile, and Brookite Polymorphs and Exploration of Surface Chemistry. *ACS Catal.* **2012**, *2*, 1817–1828. [CrossRef]

12. Zhao, J.; Li, Y.X.; Zhu, Y.; Wang, Y.; Wang, C. Enhanced CO_2 photoreduction activity of black TiO_2-coated Cu nanoparticles under visible light irradiation: Role of metallic Cu. *Appl. Catal. A* **2016**, *510*, 34–41. [CrossRef]

13. Liu, L.J.; Jiang, Y.Q.; Zhao, H.L.; Chen, J.T.; Cheng, J.L.; Yang, K.S.; Li, Y. Engineering co-exposed {001} and {101} facets in oxygen-deficient TiO_2 nanocrystals for enhanced CO_2 photoreduction under visible light. *ACS Catal.* **2016**, *6*, 1097–1108. [CrossRef]

14. Peng, C.; Reid, G.; Wang, H.F.; Hu, P. Perspective: Photocatalytic reduction of CO_2 to solar fuels over semiconductors. *J. Chem. Phys.* **2017**, *147*, 030901. [CrossRef] [PubMed]

15. IPCC. *Special Report on Carbon Dioxide Capture and Storage*; Prepared by Working Group III of the Intergovernmental Panel on Climate Change; Metz, B., Davidson, O., de Coninck, H.C., Loos, M., Meyer, L.A., Eds.; Cambridge University Press: Cambridge, UK; New York, NY, USA, 2005.

16. Wang, T.; Meng, X.; Liu, G.G.; Chang, K.; Li, P.; Kang, Q.; Liu, L.Q.; Li, M.; Ouyang, S.X.; Ye, J.H. In situ synthesis of ordered mesoporous Co-doped TiO_2 and its enhanced photocatalytic activity and selectivity for the reduction of CO_2. *J. Mater. Chem. A* **2015**, *3*, 9491–9501. [CrossRef]

17. Zhang, Q.Y.; Li, Y.; Ackerman, E.A.; Gajdardziska-Josifovska, M.; Li, H.L. Visible light responsive iodine-doped TiO_2 for photocatalytic reduction of CO_2 to fuels. *Appl. Catal. A* **2011**, *400*, 195–202. [CrossRef]

18. Sumida, K.; Rogow, D.L.; Mason, J.A.; McDonald, T.M.; Bloch, E.D.; Herm, Z.R.; Bae, T.H.; Long, J.R. Carbon Dioxide Capture in Metal–Organic Frameworks. *Chem. Rev.* **2012**, *112*, 724–781. [CrossRef] [PubMed]

19. McDonald, T.M.; Mson, J.A.; Kong, X.Q.; Bloch, E.D.; Gygi, D.; Dani, A.; Crocellà, V.; Giordanino, F.; Odoh, S.O.; Drisdell, W.S.; et al. Cooperative insertion of CO_2 in diamine-appended metal-organic frameworks. *Nature* **2014**, *519*, 303–308. [CrossRef] [PubMed]

20. Tan, H.Q.; Zhao, Z.; Niu, M.; Mao, C.Y.; Cao, D.P.; Cheng, D.J.; Feng, P.Y.; Sun, Z.C. A facile and versatile method for preparation of colored TiO_2 with enhanced solar-driven photocatalytic activity. *Nanoscale* **2014**, *6*, 10216–10223. [CrossRef] [PubMed]

21. Naldoni, A.; Allieta, M.; Santangelo, S.; Marelli, M.; Fabbri, F.; Cappelli, S.; Bianchi, C.L.; Psaro, R.; Santo, V.D. Effect of nature and location of defects on bandgap narrowing in black TiO_2 nanoparticles. *J. Am. Chem. Soc.* **2012**, *134*, 7600–7603. [CrossRef] [PubMed]

22. Janotti, A.; Varley, J.B.; Rinke, P.; Umezawa, N.; Kresse, G.; van de Walle, C.G. Hybrid functional studies of the oxygen vacancy in TiO_2. *Phys. Rev. B Condens. Matter Mater. Phys.* **2010**, *81*, 085212. [CrossRef]

23. Cronemeyer, D.C. Infrared absorption of reduced rutile TiO_2 single crystals. *Phys. Rev.* **1959**, *113*, 1222–1226. [CrossRef]

24. Yu, J.C.; Yu, G.J.; Ho, W.K.; Jiang, Z.T.; Zhang, L.Z. Effects of F-doping on the photocatalytic activity and microstructures of nanocrystalline TiO_2 powders. *Chem. Mater.* **2002**, *14*, 3808–3816. [CrossRef]

25. Xiang, Q.; Lv, K.; Yu, J. Pivotal role of fluorine in enhanced photocatalytic activity of anatase TiO_2 nanosheets with dominant (001) facets for the photocatalytic degradation of acetone in air. *Appl. Catal. B Environ.* **2010**, *96*, 557–564. [CrossRef]

26. Jiang, X.D.; Zhang, Y.P.; Jiang, J.; Rong, Y.S.; Wang, Y.C.; Wu, Y.C.; Pan, C.X. Characterization of oxygen vacancy associates within hydrogenated TiO_2: A positron annihilation study. *J. Phys. Chem. C* **2012**, *116*, 22619–22624. [CrossRef]

27. Chen, X.; Liu, L.; Peter, Y.Y.; Mao, S.S. Increasing solar absorption for photocatalysis with black hydrogenated titanium b nanocrystals. *Science* **2011**, *331*, 746–750. [CrossRef] [PubMed]

28. Zuo, F.; Bozhilov, K.; Dillon, R.J.; Wang, L.; Smith, P.; Zhao, X.; Bardeen, C.; Feng, P. Active facets on titanium(III)-doped TiO_2: An effective strategy to improve the visible-light photocatalytic activity. *Angew. Chem. Int. Ed.* **2012**, *51*, 6223–6226. [CrossRef] [PubMed]

29. Wang, Z.; Yang, C.; Lin, T.; Yin, H.; Chen, P.; Wan, D.; Xu, F.; Huang, F.; Lin, J.; Xie, X.; et al. H-doped black titania with very high solar absorption and excellent photocatalysis enhanced by localized surface plasmon resonance. *Adv. Funct. Mater.* **2013**, *23*, 5444–5450. [CrossRef]

30. Zou, X.X.; Liu, J.K.; Su, J.; Zuo, F.; Chen, J.S.; Feng, P.Y. Facile synthesis of thermal-and photostable titania with paramagnetic oxygen vacancies for visible-light photocatalysis. *Chem. Eur. J.* **2013**, *19*, 2866–2873. [CrossRef] [PubMed]

31. Venkatasubbu, G.D.; Ramakrishnan, V.; Sasirekha, V.; Ramasamy, S.; Kumar, J. Influence of particle size on the phonon confinement of TiO_2 nanoparticles. *J. Exp. Nanosci.* **2014**, *9*, 661–668. [CrossRef]

32. Zhang, W.; He, Y.; Zhang, M.; Yin, Z.; Chen, Q. Raman scattering study on anatase TiO_2 nanocrystals. *J. Phys. D Appl. Phys.* **2000**, *33*, 912–916. [CrossRef]

33. Kumar, P.M.; Badrinarayanan, S.; Sastry, M. Nanocrystalline TiO_2 studied by optical, FTIR and X-ray photoelectron spectroscopy: Correlation to presence of surface states. *Thin Solid Films* **2000**, *358*, 122–130. [CrossRef]

34. Szczepankiewicz, S.H.; Colussi, A.J.; Hoffmann, M.R. Infrared spectra of photoinduced species on hydroxylated titania surfaces. *J. Phys. Chem. B* **2000**, *104*, 9842–9850. [CrossRef]

35. Ramesha, G.K.; Brennecke, J.F.; Kamat, P.V. Origin of catalytic effect in the reduction of CO_2 at nanostructured TiO_2 films. *ACS Catal.* **2014**, *4*, 3249–3254. [CrossRef]

36. Lindan, P.; Harrison, N.; Gillan, M. Mixed dissociative and molecular adsorption of water on the rutile (110) surface. *Phys. Rev. Lett.* **1998**, *80*, 762–765. [CrossRef]

37. Bavykin, D.V.; Lapkin, A.A.; Plucinski, P.K.; Friedrich, J.M.; Walsh, F.C. Reversible Storage of Molecular Hydrogen by Sorption into Multilayered TiO_2 Nanotubes. *J. Phys. Chem. B* **2005**, *109*, 19422–19427. [CrossRef] [PubMed]

38. Nosaka, A.Y.; Fujiwara, T.; Yagi, H.; Akutsu, H.; Nosaka, Y. Photocatalytic Reaction Sites at the TiO_2 Surface as Studied by Solid-State 1H NMR Spectroscopy. *Langmuir* **2003**, *19*, 1935–1937. [CrossRef]

39. Murrell, J.N.; Sorbie, K.S. New analytic form for the potential energy curves of stable diatomic states. *J. Chem. Soc. Faraday Trans.* **1996**, *92*, 2791–2798. [CrossRef]

40. Morcombe, C.R.; Zilm, K.W. Chemical shift referencing in MAS solid state NMR. *J. Magn. Reson.* **2003**, *162*, 479–486. [CrossRef]

41. Hayashi, S.; Hayamizu, K. Chemical Shift Standards in High-Resolution Solid-State NMR (1) 13C, 29Si, and 1H Nuclei. *Bull. Chem. Soc. Jpn.* **1991**, *64*, 685–687. [CrossRef]